Detachment-parallel recharge explains high discharge fluxes at the TAG hydrothermal field

Lars Rüpke (lruepke@geomar.de)
GEOMAR Helmholtz Centre for Ocean Research Kiel https://orcid.org/0000-0001-7025-4362
Zhikui Guo
GEOMAR Helmholtz Centre for Ocean Research Kiel https://orcid.org/0000-0002-0604-0455
Sven Petersen
GEOMAR Helmholtz Centre for Ocean Research Kiel https://orcid.org/0000-0002-5469-105X
Christopher German
WHOI
Benoit Ildefonse
Géosciences Montpellier, University of Montpellier and CNRS https://orcid.org/0000-0001-7635-9288
Jörg Hasenclever
Insitute of Geophysics, University of Hamburg
Jörg Bialas
GEOMAR Helmholtz Center for Ocean Research Kiel https://orcid.org/0000-0001-8802-5277
Chunhui Tao
Second Institute of Oceanography, MNR https://orcid.org/0000-0003-3186-1447

Physical Sciences - Article

Keywords:

Posted Date: December 8th, 2021

DOI: https://doi.org/10.21203/rs.3.rs-1030743/v1

Detachment-parallel recharge explains high discharge fluxes at the TAG hydrothermal field

Zhikui Guo[1,2], Lars Rüpke[1,*], Sven Petersen[1], Christopher R German[3], Benoit Ildefonse[4], Jörg Hasenclever[5], Jörg Bialas[1], and Chunhui Tao[2,6,*]

[1]GEOMAR Helmholtz Centre for Ocean Research Kiel, Kiel, Germany
[2]Key Laboratory of Submarine Geosciences, SOA, Second Institute of Oceanography, MNR, Hangzhou, China
[3]Woods Hole Oceanographic Institution, Woods Hole, MA, USA
[4]Géosciences Montpellier, University of Montpellier and CNRS, Montpellier, France
[5]Institute of Geophysics, CEN, Hamburg University, Germany
[6]School of Oceanography, Shanghai Jiao Tong University, Shanghai, China
[*]lruepke@geomar.de, taochunhuimail@163.com

Abstract

Submarine massive sulfide deposits on slow-spreading ridges are larger and longer-lived than deposits at fast-spreading ridges[1,2], likely due to more pronounced tectonic faulting creating stable preferential fluid pathways[3,4]. The TAG hydrothermal mound at 26°N on the Mid-Atlantic Ridge (MAR) is a typical example located on the hanging wall of a detachment fault[5–7]. It has formed through distinct phases of high-temperature fluid discharge lasting 10s to 100s of years throughout at least the last 50,000 years[8] and is one of the largest sulfide accumulations on the MAR. Yet, the mechanisms that control the episodic behavior, keep the fluid pathways intact, and sustain the observed high heat fluxes of up to 1800 MW[9] remain poorly understood. Previous concepts involved long-distance channelized high-temperature fluid upflow along the detachment[5,10] but that circulation mode is thermodynamically unfavorable[11] and incompatible with TAG's high discharge fluxes. Here, based on the joint interpretation of hydrothermal flow observations and 3-D flow modeling, we show that the TAG system can be explained by episodic magmatic intrusions into the footwall of a highly permeable detachment surface. These intrusions drive episodes of hydrothermal activity with sub-vertical discharge and recharge along the detachment. This revised flow regime reconciles problematic aspects of previously inferred circulation patterns and can be used as guidance to one critical combination of parameters that can generate substantive mineral systems.

Introduction

High temperature hydrothermal discharge at *black smoker* vent sites has been reported from mid-ocean ridge segments opening at all spreading rates[12,13] and is known to play a key role in global biogeochemical cycles[14–16] as well as in the formation of massive sulfide ore deposits[1]. The style of venting, the composition of the discharged fluids, and the controls on vent field locality all appear, however, to be affected by spreading rate-dependent processes[17]. At intermediate- to fast-spreading ridges, where plate separation is compensated by magma emplacement, hydrothermal vent sites are located on-axis and hydrothermal circulation is driven by heat released from a quasi-stable melt lens modulated by periodic dike emplacement events[3,18,19]. Ultraslow to slow spreading ridges are different in that plate separation is not fully accommodated by magmatism resulting in shifting periods of magmatic- to tectonic-dominated phases of ocean spreading. Given the right balance between magmatism and tectonic extension[20–22], oceanic core complexes can form when long-lived low-angle normal faults, so-called detachment faults, accommodate large amounts of strain[20,23], and exhume lower crustal and mantle rocks. This asymmetric accretion mode is now thought to play a key role in the accretion of Atlantic-type slow-spread crust[23–25]. Where tectonic processes dominate and faulting shapes the ridge segment structure, vent sites can be located far off-axis pointing to strong links between tectonic faulting and hydrothermal circulation[26–28]. Fault-controlled hydrothermal systems also tend to be longer lived and host the largest massive sulfide deposits[1–3], which is typically explained by stable preferential pathways that large offset faults provide for hydrothermal fluid flow.

Yet, hydrothermal discharge is clearly not a steady-state process. Where it has been measured or inferred, the total heat discharge rates are much higher than the baseline mid-ocean ridge heat supply calculated from the energy loss involved in cooling the crust to approx. 350°C and crystallizing it. Baker (2007)[9] showed that the known vent fields on slow spreading ridges would need to cool segments of 13-333 km length, if steady-state were assumed. As this is implausible, hydrothermal cooling is likely highly episodic with vent fields along slow-spreading ridges only being active about 5% of the time[9], possibly paced by the frequency of magmatic intrusions. This episodic nature of hydrothermal cooling has been documented at the TAG hydrothermal field, where drilling during ODP leg 158 probed the internal structure of the mound and fairly detailed age constraints are available[29,30]. Mass-balancing the amount of sulfide at the TAG mound and the amount of fluid needed to sustain the inferred total heat discharge revealed that TAG was probably only active $< 2\%$ of its approx. 50 kyrs life time[8].

Interestingly, these two lines of argument that 1) deposits at slow-spreading ridges are larger due to long time spans of activity and 2) high discharge fluxes require cooling to be episodic, are difficult to reconcile with each other unless each phase of activity reuses the same plumbing system to form a long-lived deposit. But what critical combination of hydro-tectono-magmatic conditions is required for this to occur? Here, using the TAG hydrothermal field as an example, we identify a pattern of circulation that can sustain transient high discharge fluxes at a fault-controlled vent-system — one that has the potential to repeatedly focus hydrothermal discharge at the TAG mound over multiple cycles of activity.

The TAG hydrothermal field

The TAG hydrothermal field is located off-axis at 26°N on the eastern flank of the Mid-Atlantic Ridge (MAR). The main site of high-temperature venting is currently located at the TAG mound, where black smokers are discharging fluids at approx. 360 °C[31]. The system is highly productive with inferred energy discharge fluxes of 86 to 1,800 MW[9]; with the spread reflecting different types of measurements referring to localized discharge at the active mound or integrated total diffusive plus localized heat discharge at the TAG segment. This hydrothermal activity has resulted in the accumulation of $\sim$ 2.7 Mt of massive sulfides at the active mound and $\sim$ 20 Mt in the wider TAG area[32]. In addition to the focused high-temperature venting, widespread diffuse venting is occurring as evidenced by the abundant anhydrite within the TAG mound that likely formed through extensive mixing of hydrothermal fluids with seawater[33]. Reported ages of the TAG mound span at least 50,000 yrs showing distinct phases of high-temperature hydrothermal activity[30] with the current phase having probably started about 80 yrs ago[34]. Ages of up to 140,000 yrs have been reported for the Mir Zone on the TAG segment[30,32](Fig. 1). Those ages, in combination with the internal structure of the mound and evidence from sulfur isotopes pointing to the dissolution of anhydrite during renewed phases of high temperature activity, all support the concept of episodic activity during which fluid pathways through the TAG mound are re-activated[35]. The TAG segment is likely undergoing active detachment faulting as evidenced by microearthquake data[5], 2-D[6] as well as 3-D[36] seismic tomography, and high-resolution bathymetric data[32]. The duration of active detachment faulting is in the range of 0.35[7] to 1.35[36] Myrs. Recent high-resolution AUV-based bathymetry shows that the TAG mound is located on the hanging wall of the detachment directly at the intersection of two sets of normal faults, one parallel to the spreading direction and one oblique oriented in SW-NE direction[32](Fig. 1).

While these observations point to strong interrelations between tectonic faulting, magmatic activity, and hydrothermal flow, identifying the driving heat source has been a challenge and with it the identification of circulation pathways. Slip on the detachment, which progressively brings hotter footwall rocks closer to the surface, does not provide sufficient energy to sustain the discharge fluxes at TAG, which most likely require a magmatic heat source[6]. Two main options appear plausible: either the magmatic heat source is located beneath the neo-volcanic zone, or a magmatic intrusion in the footwall beneath TAG is driving flow. Unfortunately, seismic surveys have struggled to resolve this question. While Kong et al.[37] found a low velocity anomaly at 3-6 km depth beneath TAG, a later study by Canales et al.[6] could not identify an intrusion in the TAG footwall. However, a 3-D tomography based on the data of the same seismic survey did reveal a low velocity anomaly and a zone of inverted vertical velocity gradients beneath TAG[36], possibly in support of a magmatic footwall intrusion (see Extended Data Fig. 1d).

Based on the micro-seismicity data, deMartin et al. (2007)[5] proposed that a deep magmatic intrusion approx. 7 km beneath the neovolcanic zone drives channelized high-temperature hydrothermal flow along the detachment to below the active mound. This two-dimensional concept of channelized high temperature fluid flow along a detachment surface has been highly influential and invoked to explain off-axis venting at Logatchev[11] on the MAR and Longqi[28] on the Southwest Indian Ridge (SWIR). However, recent theoretical work showed that channelizing hot fluids over long distances along a low-angle detachment is difficult. Hot fluids tend to rise vertically due to their high buoyancy, so that strong permeability contrasts are necessary, which inevitably result in mixing processes and low vent temperatures incompatible with observations; except for very special parameter combinations[11].

An alternative flow solution is hinted at by the joint interpretation of the high-resolution bathymetry[32] and 3-D tomography data[36], which show that TAG is located at intersecting normal faults in the hanging wall and is centered above a slow seismic anomaly in the footwall (Extended Data Fig. 1). It appears plausible that flow is driven by a series of footwall magmatic intrusions with discharge being vertical in the direction of buoyancy along the cross-cutting faults in the hanging wall and recharge occurring in the third-dimension along the detachment surface. Here, using a combined analytical and numerical

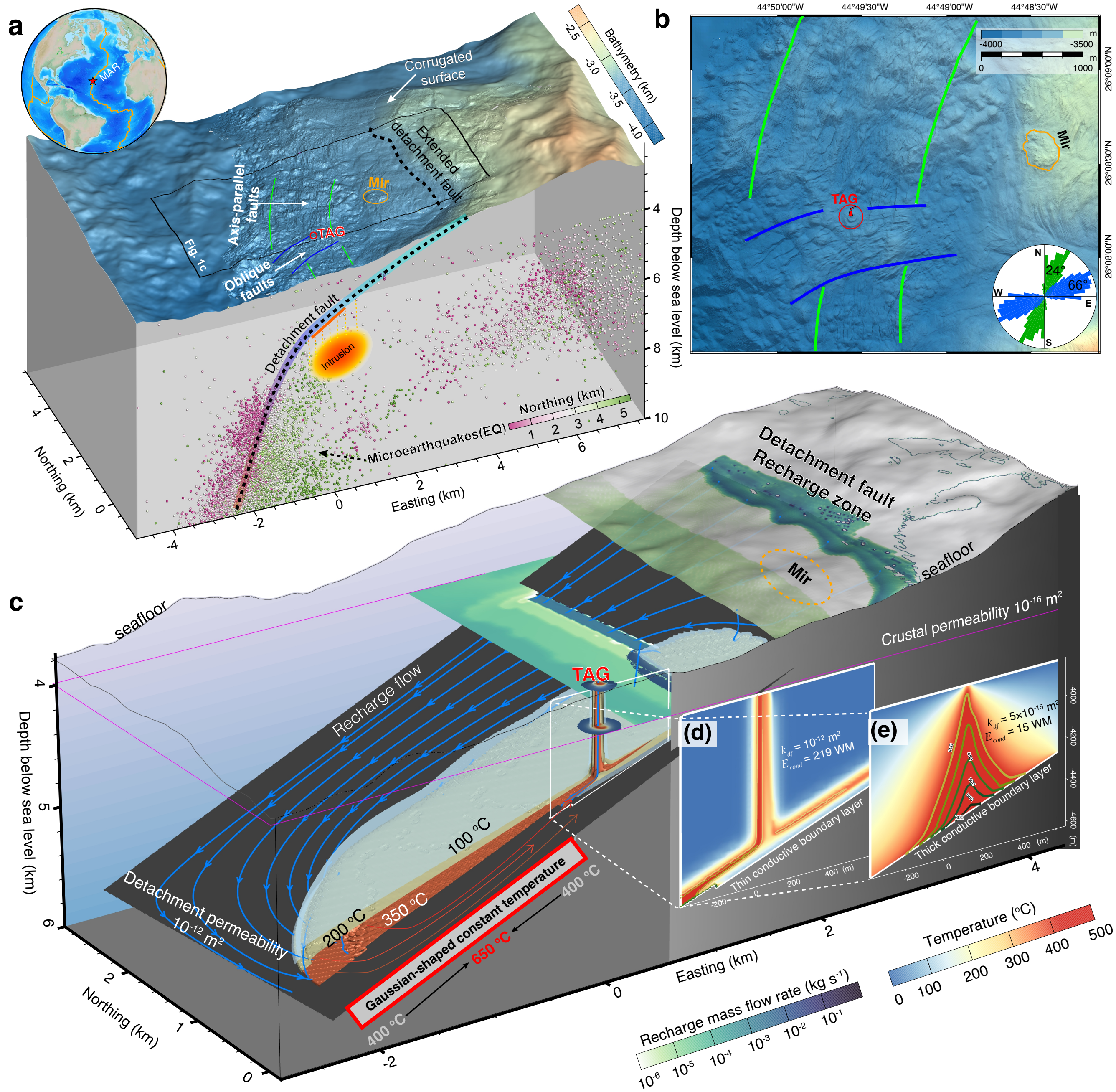

Fig. 1: The TAG hydrothermal field in models and data. a, High resolution (2m) AUV-based bathymetric data shows the location of the TAG and Mir sites, termination and corrugated surface of the detachment fault, extended detachment (black dashed line), and regions of axis-parallel (N-S) and oblique (NE-SW) faulting. The thin black box denotes lateral extent of Fig. 1c. In the sub-seafloor, dots represent location of microearthquakes[5]. The intrusion driving the current hydrothermal phase is sketched as gradient-color filled ellipse. Extended Data Fig. 1 provides further details on the sub-seafloor structure. **b,** Close-up of seafloor affected by cross-cutting normal faulting around the TAG mound and Mir Zone. The axis-parallel and oblique fault regions are bounded by green and blue lines, and their strike orientations are indicated in the inset rose diagram. **c,** Results of 3D hydrothermal flow modeling. The dark inclined plane inside the modeling domain represents the presumed detachment fault zone with incline angle 20° and thickness 50 m, the blue lines with arrows denote pathways of numerical fluid tracers. Isotherms of $100, 200, 350$ °C are shown as transparent surfaces. Recharge mass flux mainly occurs along the detachment surface. Discharge flow is vertical along a zone of enhanced permeability towards the active TAG mound. Note that only a part of the full modeling domain is shown for improved readability. The complete fluid velocity field is shown in Supplementary Fig.3. **d** and **e** show the temperature field on vertical profiles across the TAG vent for $k_{df} = 10^{-12}\ m^2$ and $5 \times 10^{-15}\ m^2$, respectively. Energy discharge increases for higher detachment fault permeability due to a thinner thermal boundary layer.

approach, we show that this flow solution is robust and stable over a large parameter range and that its magmatic-tectonic ingredients may represent a critical combination of parameters that make the TAG mineral system so prolific.

Results

To explore the likely circulation pattern during phases of high temperature hydrothermal discharge, we use the three-dimensional hydrothermal flow model HydrothermalFoam[38], which resolves porous convection of pure water under single-phase conditions. Based on the high-resolution AUV-bathymetry[32], micro-earthquake locations[5], and tomographic[36] plus seismic reflection[39] data, we implement the detachment surface as an inclined permeable plane dipping at 20°. Here the assumption is that the detachment surface is a zone of enhanced permeability with respect to the adjacent foot- and hanging walls[40]. The cross-cutting faults at TAG are simplified as a pipe- or slot-shaped zone (Supplementary Fig. 1) of enhanced permeability that we assume intersects the detachment surface approx. 700 m below the seafloor. The presumed driving heat source in the detachment footwall is implemented as a Gaussian-shaped fixed temperature boundary condition (see Methods). Fig. 1 summarizes the model setup and likely circulation mode: segment-scale down-flow of cold seawater occurs along the permeable detachment and recharges the reaction zone beneath TAG from where high-temperature discharge flow is mainly vertical. This three-dimensional circulation mode is fundamentally different to previous ideas involving long-distant hydrothermal upflow from a deep magmatic heat source near the ridge axis along the detachment towards the TAG mound. First, heat is extracted directly across a thin thermal boundary layer from the footwall beneath TAG into the highly permeable detachment flow zone. This makes hydrothermal heat extraction highly efficient as the thickness of the thermal boundary layer is directly related to the permeability of the reaction zone[41]. Second, extensive three-dimensional along-fault flow mines heat from a large spatial extent and further increases the hydrothermal heat output. And finally, our proposed flow model does not involve channelizing hot fluids laterally over long distances against the direction of buoyancy-driven flow.

To further explore the general behavior of the proposed circulation system in terms of the predicted vent temperatures, vent location, and power output, we have performed a sequence of 3-D numerical experiments changing model parameters and geometry. In addition we have derived a semi-analytical solution for the theoretical power output. Fig. 1d and e exemplify the effects of changing the permeability of the detachment fault. Within the reaction zone, where a constant temperature boundary condition is applied, heat is transferred by conduction from the intrusion into the hydrothermal flow zone across a thermal boundary layer. The total conductive heat input (E_{cond}) is a function of heat source temperature and boundary layer thickness, over which temperature decreases to approx. 400°C. This thickness is controlled by the permeability of the reaction zone. In the case of a highly permeable detachment ($k_{df} = 10^{-12}\ m^2$), the total conductive heat input is 219 MW (Fig. 1d). If k_{df} is reduced to $5 \times 10^{-15}\ m^2$, the conductive boundary layer is thicker and the heat input is reduced to 15 MW (Fig. 1e). Hence the total heat output scales with reaction zone permeability, which implies that having the heat source close to the permeable flow zone is an effective way to increase the total heat output of a circulation system (see ref.[41] for theoretical background).

The impact of parameter values on heat extraction and flow pattern is further illustrated in Fig. 2, which shows the flow solution and some characteristics of it for differing detachment fault and upflow zone permeabilities. Fig. 2a shows the results for a model run that defines the upflow zone as a permeable pipe in which the detachment fault is twice as permeable as the pipe. About 85% of recharge mass flow occurs via the detachment and approx. 65% of the discharge occurs via the pipe, which is mainly used for discharge flow. Vent temperature is high at approx. 405°C. If the pipe permeability is increased by a factor of 4 (Fig. 2b), the pipe is used for both recharge and discharge flow, which results in a reduced vent temperature due to mixing within the upflow zone. Increasing the detachment fault permeability (Fig. 2c) makes recharge via the detachment the preferred circulation mode again and the pipe is used almost exclusively for discharge. Finally, if the geometric representation of the upflow zone is changed from pipe to slot, the slot is used for recharge and discharge flow. Interestingly, this does not significantly affect vent temperatures because of less efficient mixing in the slot-like geometry. We have run simulations for a wide range of parameters and results are summarized in Fig. 3. These simulations show that segment-scale recharge occurs in all simulations and that detachment fault permeability controls conductive heat transfer into the hydrothermal flow zone. Vent temperatures are highest when the vertical flow zone is mainly used for discharge flow. When k_{df} is in the range of 2×10^{-13} to $10^{-12}\ m^2$, the total heat output spans $50 \sim 80$ MW (Fig. 3 a,b), which is in excellent agreement with the inferred heat flux of 50-86 MW for the active high temperature system[42]. These preferred absolute permeability values make the model predictions consistent with observed heat discharge fluxes as well vent exit temperatures and fall within the 10^{-14} to $10^{-12}\ m^2$ range typically reported for shallow ocean crust[43]. However, as cautious note, it should be added that the subsurface permeability structure of the highly faulted TAG segment is likely more complex and is likely to sustain more diffusive low-temperature flow. Our simplified model setup was designed to capture the key flow characteristics of the focused high temperature circulation system.

To evaluate the robustness of our findings, we have derived a semi-analytical solution for the power output of a hydrothermal system driven by a detachment footwall intrusion following the rationale of Jupp and Schultz[41,44]. While this simplified model (see method section) cannot capture all the complexity of a three-dimensional flow, it does confirm our key conclusion that the power output is primarily a function of reaction zone permeability, and it shows the same scaling as the numerical model (Extended Data Fig. 4).

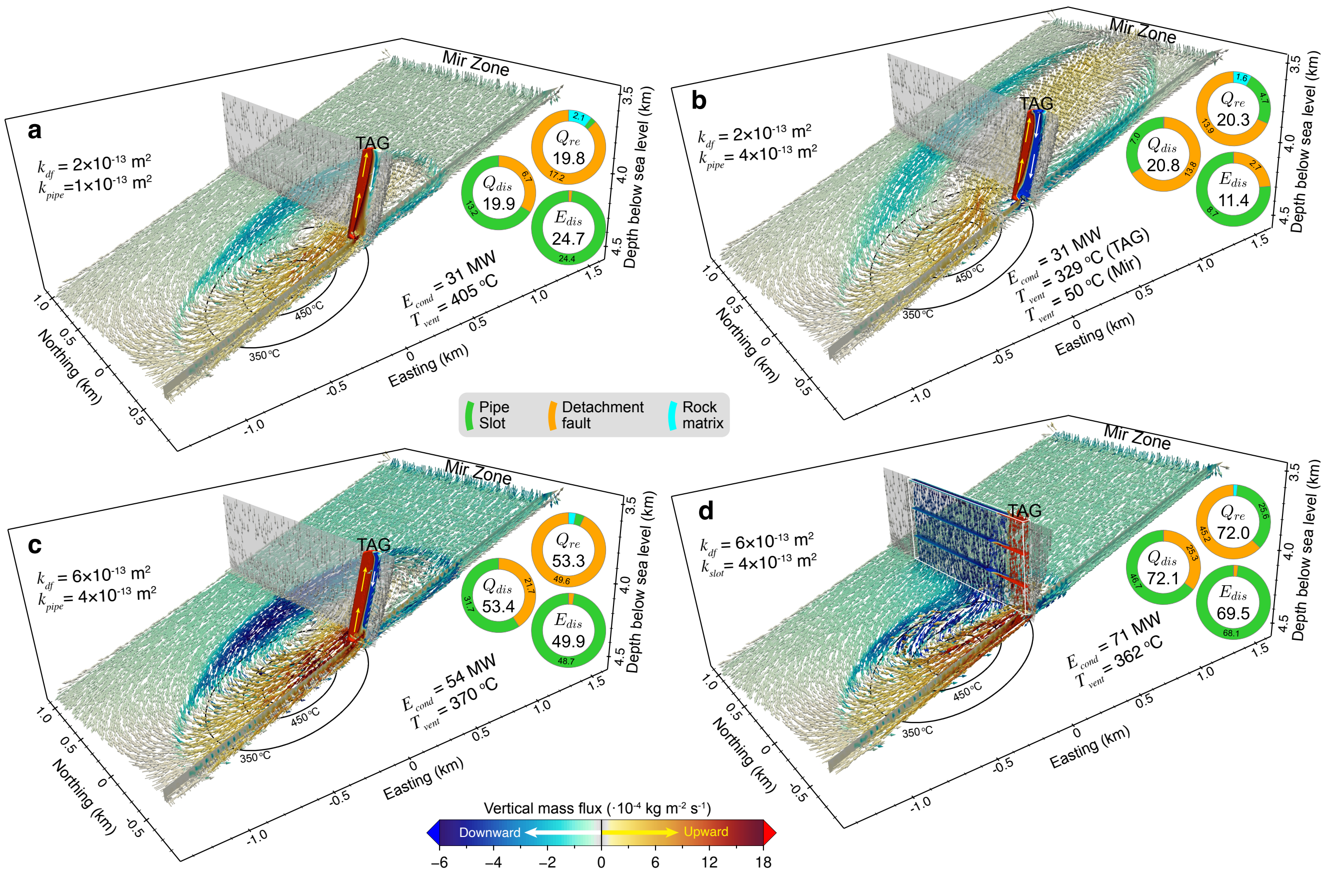

Fig. 2: 3-D flow pattern and hydrothermal power output. Vectors illustrate the three-dimensional circulation pattern and are color-coded by the vertical mass flux. Up- and downward flow along the pipe and slot are illustrated by yellow and white arrows. Pie charts show the integrated mass flow rate of recharge (Q_{re}: $kg\ s^{-1}$) and discharge (Q_{dis}: $kg\ s^{-1}$), and hydrothermal power output (E_{dis}: MW) at the seafloor. The number in each pie chart is the total value of the corresponding quantity. Wedges in each pie chart represent the proportion of flow through pipe/slot (green), detachment fault (orange), and background rock matrix (cyan). Comparing **a** and **b** on a like for like basis show that increasing k_{pipe}, the permeability of the upflow zone, results in mixing and a decrease in vent temperature. Comparing **b** and **c** shows that increasing the detachment permeability k_{df} dramatically increases the discharge flow, which reduces mixing in the upflow zone so that the vent temperature is increased, also the power output is increased. Comparing **c** and **d** illustrates the effects of changing the upflow zone geometry from pipe-like to slot-like; additional recharge flow occurs and the total power output is increased by 40%.

Discussion

The presented flow solutions illustrate the likely circulation pattern during phases of high temperature fluid discharge at TAG. The fundamental difference to previous concepts[5,11,28] on fault-controlled circulation systems is that in our new model the detachment fault is used for recharge instead of discharge flow. This circulation mode naturally forms in three-dimensional numerical models that allow for in-plane fault flow (as opposed to previously proposed two-dimensional scenarios). Discharge flow is mainly vertical and channelized towards the TAG mound by the cross-cutting normal faults in the hanging wall. A key feature of this circulation system is that the permeable detachment does not "capture" and deviate a hydrothermal plume rising through relatively low permeability rocks from a heat source at depth, which would lead to a low power output. Rather, circulation is directly driven by conductive heat input from a footwall intrusion into the hydrothermal flow zone, which leads to a high predicted power output because it scales with the high detachment permeability. Hence, the observed high power output

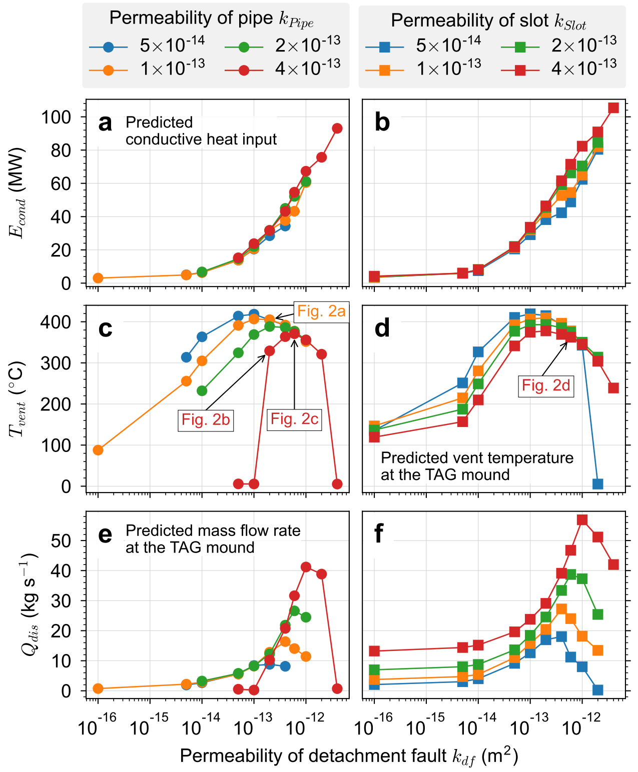

Fig. 3: Impact of parameter variations on predicted hydrothermal flow solution. The left panel refers to cross-cutting faults being represented as a pipe-like zone of enhanced permeability of 100 m diameter, while the right panel refers to a slot-shaped zone of enhanced permeability that is 50-m-wide and 1200 m long. X-axis shows changes in detachment fault permeability and colors refer to different upflow zone permeabilities. **a,b** show how conductive heat input scales with detachment permeability due to its control on thermal boundary layer thickness. **c,d** illustrate the impact on vent temperature and **e,f** illustrate how the mass discharge rate at the TAG mound increases with increasing flow zone permeability.

of some fault controlled systems – including TAG – seems to require a high conductive heat input into the hydrothermal flow zone, which implies a thin conductive boundary layer and thus a high near-intrusion permeability. In addition, this circulation mode is also the thermodynamically more plausible solution as it does not require deviating highly buoyant hydrothermal fluids against the gravitational gradient into a low-angle detachment. A corollary is that beneath TAG high temperature fluid-rock interaction within the detachment mainly occurs close to the heat source in the footwall and not because of long-distance channelized flow along it. This would also be consistent with recent findings based on fluid inclusion data from a corrugated detachment fault on the MAR at 13°20′N[45], where a clear link between deformation and high temperature fluid rock interaction was established. However, the conclusion was drawn that this interaction happened within a reaction zone at depth, which was later exhumed by faulting.

While the presented numerical results are consistent with the available data on the current phase of hydrothermal activity, they do not directly explain the episodic nature of the TAG hydrothermal system. As aforementioned, the TAG mound has been episodically active since approx. 50,000 yrs with each phase lasting 10s - 100s of years. It appears plausible that these phases are paced by the frequency of intrusive magmatic events. Recent 3-D seismic data on the Rainbow hydrothermal field on the MAR imaged a large number of sill intrusions in the footwall of a presumed detachment surface[46]. Similar ideas on numerous footwall intrusions were presented for the Atlantis Massif on the MAR[47]. Unfortunately, constraining the timing of intrusive events remains a challenge. Yet, intrusion frequencies of several thousand to ten thousands of years appear plausible[48]. A reasonable number for the total heat required to "make" the active TAG mound is 2×10^{19} J based on the massive sulfide accumulation size and volume of hot fluids needed to form it[8]. This energy can be converted into a total magma volume of 4.3 km^3. If TAG has formed by ten hydrothermal phases, each phase would on average be driven, as described above, by at least a 0.43 km^3-sized intrusion. During each of these phases, the discharge pathways towards the TAG mound would need to be re-activated. The current seafloor morphology suggests that cross-cutting normal faults act as conduits for hydrothermal discharge[32]. However, for these pathways to be re-activated and not be replaced by other preferential pathways, the hanging wall must not have experienced significant tectonic deformation throughout the life time of the TAG mound. One plausible explanation is that extension is mainly accommodated by the detachment and possibly by magmatic accretion at the ridge-axis, so that the hanging wall did not experience strong recent deformation.

An active highly permeable detachment that allows for efficient heat extraction from magmatic footwall intrusions, in combination with stable preferential pathways in the hanging wall that are re-activated throughout multiple phases of hydrothermal discharge, may therefore be the ingredients facilitating the formation of large massive sulfide deposits at detachment-associated hydrothermal systems such as TAG. The Longqi hydrothermal field on the SWIR[49], located also on the hanging wall of a presumed detachment, may be another example, where such an interplay results in large sulfide accumulations. However, other detachment-associated vent fields like Rainbow[27] or the von Damm vent field[50] are located on exhumed footwall rocks. How and if detachment faulting affects the circulation pathways of those vent fields cannot be directly predicted using our proposed flow model for TAG-like systems.

References

1 Hannington, M., Jamieson, J., Monecke, T., Petersen, S. & Beaulieu, S. The abundance of seafloor massive sulfide deposits. *Geology* **39**, 1155–1158, DOI: 10.1130/g32468.1 (2011).

2 German, C. R., Petersen, S. & Hannington, M. D. Hydrothermal exploration of mid-ocean ridges: where might the largest sulfide deposits be forming? *Chem. Geol.* **420**, 114–126, DOI: 10.1016/j.chemgeo.2015.11.006 (2016).

3 Jamieson, J. W., Clague, D. A. & Hannington, M. D. Hydrothermal sulfide accumulation along the Endeavour Segment, Juan de Fuca Ridge. *Earth Planet. Sci. Lett.* **395**, 136–148, DOI: 10.1016/j.epsl.2014.03.035 (2014).

4 German, C. *et al.* Hydrothermal exploration near the Azores Triple Junction: tectonic control of venting at slow-spreading ridges? *Earth Planet. Sci. Lett.* **138**, 93–104, DOI: 10.1016/0012-821X(95)00224-Z (1996).

5 deMartin, B. J., Sohn, R. A., Pablo Canales, J. & Humphris, S. E. Kinematics and geometry of active detachment faulting beneath the Trans-Atlantic Geotraverse (TAG) hydrothermal field on the Mid-Atlantic Ridge. *Geology* **35**, 711–714, DOI: 10.1130/G23718A.1 (2007).

6 Canales, J. P., Sohn, R. A. & DeMartin, B. J. Crustal structure of the Trans-Atlantic Geotraverse (TAG) segment (Mid-Atlantic Ridge, 26°10'N): Implications for the nature of hydrothermal circulation and detachment faulting at slow spreading ridges. *Geochem. Geophys. Geosystems* **8**, 1–18, DOI: 10.1029/2007GC001629 (2007).

7 Tivey, M. A., Schouten, H. & Kleinrock, M. C. A near-bottom magnetic survey of the Mid-Atlantic Ridge axis at 26°N: Implications for the tectonic evolution of the TAG segment. *J. Geophys. Res. Solid Earth* **108**, DOI: 10.1029/2002JB001967 (2003).

8 Humphris, S. E. & Cann, J. R. Constraints on the energy and chemical balances of the modern TAG and ancient Cyprus seafloor sulfide deposits. *J. Geophys. Res. Solid Earth* **105**, 28477–28488, DOI: 10.1029/2000JB900289 (2000).

9 Baker, E. T. Hydrothermal cooling of midocean ridge axes: Do measured and modeled heat fluxes agree? *Earth Planet. Sci. Lett.* **263**, 140–150, DOI: 10.1016/j.epsl.2007.09.010 (2007).

10 McCaig, A. M. & Harris, M. Hydrothermal circulation and the dike-gabbro transition in the detachment mode of slow seafloor spreading. *Geology* **40**, 367–370, DOI: 10.1130/G32789.1 (2012).

11 Andersen, C., Rüpke, L., Hasenclever, J., Grevemeyer, I. & Petersen, S. Fault geometry and permeability contrast control vent temperatures at the Logatchev 1 hydrothermal field, Mid-Atlantic Ridge. *Geology* **43**, 51–54, DOI: 10.1130/G36113.1 (2015).

12 Baker, E. T. & German, C. R. *On the Global Distribution of Hydrothermal Vent Fields*, vol. 148, 318 (American Geophysical Union, Washington DC, 2004).

13 Beaulieu, S. E., Baker, E. T. & German, C. R. Where are the undiscovered hydrothermal vents on oceanic spreading ridges? *Deep. Res. Part Ii-Topical Stud. Oceanogr.* **121**, 202–212, DOI: 10.1016/j.dsr2.2015.05.001 (2015).

14 Resing, J. A. *et al.* Basin-scale transport of hydrothermal dissolved metals across the South Pacific Ocean. *Nature* **523**, 200–203, DOI: 10.1038/nature14577 (2015).

15 German, C. R. *et al.* Hydrothermal impacts on trace element and isotope ocean biogeochemistry. *Philos. Transactions Royal Soc. a-Mathematical Phys. Eng. Sci.* **374**, DOI: ARTN2016003510.1098/rsta.2016.0035 (2016).

16 Tagliabue, A. *et al.* Hydrothermal contribution to the oceanic dissolved iron inventory. *Nat. Geosci.* **3**, 252–256, DOI: 10.1038/Ngeo818 (2010).

[17] Baker, E. T., Chen, Y. J. & Morgan, J. P. The relationship between near-axis hydrothermal cooling and the spreading rate of mid-ocean ridges. *Earth Planet. Sci. Lett.* **142**, 137–145 (1996).

[18] Coumou, D., Driesner, T. & Heinrich, C. A. The structure and dynamics of mid-ocean ridge hydrothermal systems. *Science* **321**, 1825–1828, DOI: 10.1126/science.1159582 (2008).

[19] Hasenclever, J. *et al.* Hybrid shallow on-axis and deep off-axis hydrothermal circulation at fast-spreading ridges. *Nature* **508**, 508–512, DOI: 10.1038/nature13174 (2014).

[20] Buck, W. R., Lavier, L. L. & Poliakov, A. N. B. Modes of faulting at mid-ocean ridges. *Nature* **434**, 719–723, DOI: 10.1038/nature03358 (2005).

[21] Tucholke, B. E., Behn, M. D., Buck, W. R. & Lin, J. Role of melt supply in oceanic detachment faulting and formation of megamullions. *Geology* **36**, 455, DOI: 10.1130/g24639a.1 (2008).

[22] Olive, J.-A., Behn, M. D. & Tucholke, B. E. The structure of oceanic core complexes controlled by the depth distribution of magmaăemplacement. *Nat. Geosci.* **3**, 491–495, DOI: 10.1038/ngeo888 (2010).

[23] Escartin, J. *et al.* Central role of detachment faults in accretion of slow-spreading oceanic lithosphere. *Nature* **455**, 790–U5, DOI: 10.1038/nature07333 (2008).

[24] Bialas, J., Dannowski, A. & Reston, T. J. Interplay between magmatic accretion, spreading asymmetry and detachment faulting at a segment end: Crustal structure south of the Ascension Fracture Zone. *Earth Planet. Sci. Lett.* **432**, 84–94, DOI: 10.1016/j.epsl.2015.09.027 (2015).

[25] Cann, J. R. *et al.* Corrugated slip surfaces formed at ridge-transform intersections on the Mid-Atlantic Ridge. *Nature* **385**, 329–332, DOI: DOI10.1038/385329a0 (1997).

[26] Petersen, S. *et al.* The geological setting of the ultramafic-hosted Logatchev hydrothermal field (14°45′N, Mid-Atlantic Ridge) and its influence on massive sulfide formation. *Lithos* **112**, 40–56, DOI: 10.1016/j.lithos.2009.02.008 (2009).

[27] Andreani, M. *et al.* Tectonic structure, lithology, and hydrothermal signature of the Rainbow massif (Mid-Atlantic Ridge 36°14'N). *Geochem. Geophys. Geosystems* **15**, 3543–3571, DOI: 10.1002/2014GC005269 (2014).

[28] Tao, C. *et al.* Deep high-temperature hydrothermal circulation in a detachment faulting system on the ultra-slow spreading ridge. *Nat Commun* **11**, 1300, DOI: 10.1038/s41467-020-15062-w (2020).

[29] Humphris, S. E. *et al.* The Internal Structure of an Active Sea-Floor Massive Sulfide Deposit. *Nature* **377**, 713–716, DOI: DOI10.1038/377713a0 (1995).

[30] Lalou, C., Reyss, J.-L., Brichet, E., Rona, P. A. & Thompson, G. Hydrothermal activity on a 10 5 -year scale at a slow-spreading ridge, TAG hydrothermal field, Mid-Atlantic Ridge 26°N. *J. Geophys. Res. Solid Earth* **100**, 17855–17862, DOI: 10.1029/95JB01858 (1995).

[31] Edmond, J. *et al.* Time series studies of vent fluids from the TAG and MARK sites (1986, 1990) Mid-Atlantic Ridge: a new solution chemistry model and a mechanism for Cu/Zn zonation in massive sulphide orebodies. *Geol. Soc. London, Special Publ.* **87**, 77–86, DOI: 10.1144/GSL.SP.1995.087.01.07 (1995).

[32] Graber, S. *et al.* Structural control, evolution, and accumulation rates of massive sulfides in the TAG hydrothermal field. *Geochem. Geophys. Geosystems* **21**, e2020GC009185, DOI: 10.1029/2020GC009185 (2020).

[33] Humphris, S. E., Tivey, M. K. & Tivey, M. A. The Trans-Atlantic Geotraverse hydrothermal field: A hydrothermal system on an active detachment fault. *Deep. Sea Res. Part II: Top. Stud. Oceanogr.* **121**, 8–16, DOI: 10.1016/j.dsr2.2015.02.015 (2015).

[34] Lalou, C. *et al.* New age data for Mid-Atlantic Ridge hydrothermal sites: TAG and Snakepit chronology revisited. *J. Geophys. Res. Solid Earth* **98**, 9705–9713, DOI: 10.1029/92JB01898 (1993).

[35] Petersen, S., Herzig, P. & Hannington, M. D. Third dimension of a presently forming VMS deposit: TAG hydrothermal mound, Mid-Atlantic Ridge, 26 N. *Miner. Deposita* **35**, 233–259, DOI: 10.1007/s001260050018 (2000).

[36] Zhao, M., Canales, J. P. & Sohn, R. A. Three-dimensional seismic structure of a Mid-Atlantic Ridge segment characterized by active detachment faulting (Trans-Atlantic Geotraverse, 25°55′N-26°20′ N). *Geochem. Geophys. Geosystems* **13**, DOI: 10.1029/2012GC004454 (2012).

[37] Kong, L. S. L., Solomon, S. C. & Purdy, G. M. Microearthquake Characteristics of a Mid-Ocean Ridge along-axis high. *J. Geophys. Res. Solid Earth* **97**, 1659–1685, DOI: https://doi.org/10.1029/91JB02566 (1992).

[38] Guo, Z., Rüpke, L. & Tao, C. HydrothermalFoam v1. 0: a 3-D hydrothermal transport model for natural submarine hydrothermal systems. *Geosci. Model. Dev.* **13**, 6547–6565, DOI: 10.5194/gmd-13-6547-2020 (2020).

[39] Szitkar, F. *et al.* Detachment tectonics at Mid-Atlantic Ridge 26° N. *Sci. reports* **9**, 1–8, DOI: 10.1038/s41598-019-47974-z (2019).

[40] Kopf, A. Permeability variation across an active low-angle detachment fault, western Woodlark Basin (ODP Leg 180), and its implication for fault activation. *Geol. Soc. London, Special Publ.* **186**, 23–41, DOI: 10.1144/GSL.SP.2001.186.01.03 (2001).

[41] Jupp, T. E. & Schultz, A. Physical balances in subseafloor hydrothermal convection cells. *J. Geophys. Res. Solid Earth* **109**, DOI: 10.1029/2003JB002697 (2004).

[42] Goto, S., Kinoshita, M., Schultz, A. & Von Herzen, R. P. Estimate of heat flux and its temporal variation at the TAG hydrothermal mound, Mid-Atlantic Ridge 26°N. *J. Geophys. Res. Solid Earth* **108**, DOI: 10.1029/2001JB000703 (2003).

[43] Fisher, A. T. Permeability within basaltic oceanic crust. *Rev. Geophys.* **36**, 143–182, DOI: 10.1029/97RG02916 (1998).

[44] Jupp, T. & Schultz, A. A thermodynamic explanation for black smoker temperatures. *Nature* **403**, 880–883, DOI: 10.1038/35002552 (2000).

[45] Verlaguet, A. *et al.* Fluid Circulation Along an Oceanic Detachment Fault: Insights From Fluid Inclusions in Silicified Brecciated Fault Rocks (MidAtlantic Ridge at 13°20'N). *Geochem. Geophys. Geosystems* **22**, DOI: 10.1029/2020gc009235 (2021).

[46] Dunn, R. A., Arai, R., Eason, D. E., Canales, J. P. & Sohn, R. A. Three-Dimensional Seismic Structure of the Mid-Atlantic Ridge: An Investigation of Tectonic, Magmatic, and Hydrothermal Processes in the Rainbow Area. *J. Geophys. Res. Earth* **122**, 9580–9602, DOI: 10.1002/2017jb015051 (2017).

[47] Grimes, C. B., John, B. E., Cheadle, M. J. & Wooden, J. L. Protracted construction of gabbroic crust at a slow spreading ridge: Constraints from^{206}Pb/^{238}U zircon ages from Atlantis Massif and IODP Hole U1309D (30°N, MAR). *Geochem. Geophys. Geosystems* **9**, 1–24, DOI: 10.1029/2008gc002063 (2008).

[48] Fan, Q., Olive, J. & Cannat, M. ThermoMechanical State of UltraslowSpreading Ridges With a Transient Magma Supply. *J. Geophys. Res. Solid Earth* **126**, DOI: 10.1029/2020jb020557 (2021).

[49] Tao, C. *et al.* First active hydrothermal vents on an ultraslow-spreading center: Southwest Indian Ridge. *Geology* **40**, 47–50, DOI: 10.1130/G32389.1 (2012).

[50] Haughton, G., Hayman, N., Searle, R., Le Bas, T. & Murton, B. Volcanic-tectonic structure of the Mount Dent oceanic core complex in the ultraslow Mid-Cayman Spreading Center determined from detailed seafloor investigation. *Geochem. Geophys. Geosystems* **20**, 1298–1318, DOI: 10.1029/2018GC008032 (2019).

Methods

Governing equations and numerical method

We model the hydrothermal convection as buoyant Darcy flow in a porous medium using the novel hydrothermal flow modeling framework HydrothermalFoam[38], which is based on OpenFOAM[51]. This model framework can handle complex geometries in both 2-D and 3-D and has been designed for massively parallel computations. HydrothermalFoam solves the equations of mass conservation and energy conservation using the finite-volume method and calculates fluid velocities using Darcy's law according to:

$$\vec{U} = -\frac{k}{\mu_f}(\nabla p - \rho_f \vec{g}) \tag{1}$$

k denotes permeability, p total fluid pressure, $\vec{g}$ gravitational acceleration, μ_f and ρ_f are the fluid's dynamic viscosity and density, respectively. Considering a compressible fluid in a porous medium with given porosity structure, the mass balance is expressed by

$$\varepsilon \frac{\partial \rho_f}{\partial t} + \nabla \cdot (\vec{U}\rho_f) = 0 \tag{2}$$

where ε is the porosity of the rock. Note that we assume the matrix to be incompressible, so that the porosity is outside the time derivative. The equation for pressure can be derived by substituting Darcy's law (Equation 1) into the continuity equation (2) and treating the fluid's density as a function of temperature T and pressure p:

$$\varepsilon \rho_f \left(\beta_f \frac{\partial p}{\partial t} - \alpha_f \frac{\partial T}{\partial t}\right) = \nabla \cdot \left(\rho_f \frac{k}{\mu_f}(\nabla p - \rho_f \vec{g})\right) \tag{3}$$

with α_f and β_f being the fluid's thermal expansivity and compressibility, respectively. Again there is no rock compressibilty as we consider the incompressible matrix case. Energy conservation of a single-phase fluid can be expressed using a temperature formulation[19,38],

$$(\varepsilon\rho_f C_{pf} + (1-\varepsilon)\rho_r C_{pr})\frac{\partial T}{\partial t} = \nabla\cdot(\lambda_r \nabla T) - \rho_f C_{pf}\vec{U}\cdot\nabla T + \frac{\mu_f}{k}\parallel \vec{U} \parallel^2 - \left(\frac{\partial ln\rho_f}{\partial lnT}\right)_p \left(\varepsilon\frac{\partial p}{\partial t} + \vec{U}\cdot\nabla p\right) \tag{4}$$

Thermodynamic properties of fluids, i.e. water, are calculated using the IAPWS-IF97 formulation[52,53], that provides the fluid properties as nonlinear functions of temperature and pressure. All the symbols and their physical meanings and typical values can be found in Supplementary Table 1.

Initial and boundary conditions of the 3D model

The model geometry is based on geophysical data. Seafloor information such as total heat discharge and vent temperatures are used for model calibration. The geometry of the detachment fault is based on high-resolution bathymetric data[32] and P-wave velocity analysis[36]. According to the estimation of the detachment fault thickness ($70-100$ m) in previous studies one TAG[36,45] and seismic evidence for detachment fault thickness ($33.4\pm5.7m$) in Wooodlark basin[54], we set it to be 50 m. In addition, the numerical model is based on the hypothesis that the TAG hydrothermal system is driven by shallow intrusion(s). We therefore only consider the shallow part of the detachment[36] down to a depth of 6 km below sea level. The 3D model is constructed in a box laterally bounded by south-west point (44°51.6′ W, 26°6.8′ N) and north-east point (44°47′ W, 26°9.8′ N), corresponding to lateral extent of 5.6 km to the north and 7.8 km to the east. This geometry allows for free 3-D flow patterns to emerge that are not strongly affected by the domain sidewalls (see Supplementary Fig. 1 for the complete geometry setup). All side boundaries are impermeable and insulating. The top boundary is constrained by shipbased bathymetry (30 m grid resolution) acquired during cruise M127. A Dirichlet boundary condition of pressure is applied on top boundary of the domain, i.e. seafloor, and the fixed value is calculated as hydrostatic pressure according to the bathymetry data. For temperature on the top boundary, we use a mixed boundary conditions where temperature is set to a seawater temperature of 2 °C where fluids enter the domain, and at locations where fluids leave the domain the temperature gradient is set to zero ($\partial T/\partial\vec{n} = 0$) to allow for free venting conditions. The footwall heat source is approximates as a gaussian shaped constant temperature boundary condition with temperatures varying between $400-650$ °C. The bottom boundary is impermeable. All model runs start from initially cold conditions and evolve towards the (pseudo) steady-state solutions. The porosity of all the models are kept at a constant value of 10%, which is a rough average value from seismic velocity-porosity relationship of TAG samples[55]. Permeability of background wall rocks (adjacent foot- and hanging walls) is set to 10^{-16} m^2 based on previous studies[11,28,43], and is kept constant for all numerical experiments.

Meshing and parallel computing

The 3D model domain is discretized into a polyhedral mesh using OpenFOAM's internal tool *snappyHexMesh*. In order to resolve flow field in detail, the mesh size in detachment fault zone and shallow tectonic zone (pipe or slot) where fluid temperature, pressure and velocity have large variation, is refined to a high resolution of up to 5 m.The mesh size of background rock matrix is approx. 50 m. The whole 3D model is meshed with $\sim$ 12 million polyhedron elements. Based on the Courant-Friedrichs-Lewy (CFL) condition, which relates flow speed to numerical resolution, the time step is automatically updated and ranges from $\sim$ 22 hours to $\sim$ 50 days for higher permeability model (e.g., $k_{df} = 10^{-12}$ m^2) and lower permeability model (e.g., $k_{df} = 10^{-14}$ m^2), respectively. Benefitting from the excellent parallel performance of the OpenFOAM framework, we decompose the 3D model domain into N sub-domains (see Extended Data Fig. 2) in which the equations can be solved in parallel by N processors. In addition, every point in Fig. 3 represents a 3D model with different parameters. Every model is solved with 50 processors and takes a computing time of $\sim$4 days to reach a quasi-steady state.

Analysis of mass flux and heat power output

All analyses are done based on the modeling results at a quasi-steady state, which is determined from variations of total recharge (Q_{re} in Equation 5) and discharge (Q_{dis} in Equation 6) mass flux, and vent temperature (T_{vent}). A model can be regarded as reaching to quasi-steady state when the magnitude of Q_{re} and Q_{dis} are approximately equal and tend to be constant, and T_{vent} tends to be constant as well. For seafloor or other slices, the integrated mass flow rate can be calculated as,

$$Q_{re} = \sum_{face=1}^{N} \rho_f \vec{U} \cdot \vec{S}_{face} \;\; (\vec{U} \cdot \vec{g} > 0, \;\text{recharge flow}) \tag{5}$$

$$Q_{dis} = \sum_{face=1}^{N} \rho_f \vec{U} \cdot \vec{S}_{face} \;\; (\vec{U} \cdot \vec{g} < 0, \;\text{discharge flow}) \tag{6}$$

where $\vec{S}_{face}$ is the surface vector of the $face$ with magnitude of face area and pointing outside of the 3D model domain, N is the number of faces. Based on the specific enthalpy (H_f) of the fluids, calculated from IAPWS-IF97, the total discharge heat output can be calculated as

$$E_{dis} = \sum_{face=1}^{N} \rho_f (H_f - H_0) \vec{U} \cdot \vec{S}_{face} \;\; (\vec{U} \cdot \vec{g} < 0, \;\text{discharge flow}) \tag{7}$$

with H_0 being specific enthalpy of seawater with temperature 2 °C.

Conductive heat power is calculated from temperature gradient at conductive boundary $patch$ (heat source boundary) based on Fourier's law of heat transfer,

$$E_{cond} = \sum_{patch=1}^{N} -\lambda_r \vec{S}_{patch} \cdot \nabla T \tag{8}$$

Likewise, $\vec{S}_{patch}$ is the surface vector of conductive boundary $patch$ (face) with magnitude of patch area and orientation outside of the 3D model domain. For example, Q_{dis}, T_{vent} and E_{cond} through seafloor of each 3D model are summarized in Fig. 3.

Scaling analysis of total advective heat power

To obtain a general quantitative relationship between total advective heat power (how much heat can be extracted from the heat source), heat source geometry, permeability, and geometry of detachment fault zone and shallow tectonic structure, we use the scaling analysis method[41] to derive an analytical solution based on a simplified detachment-pipe model (see Extended Data Fig. 3). The model is composed of (1) a detachment fault zone with incline angle α, thickness H_R, extensional length L_z in the third direction (z axis), and permeability k_R; (2) an elliptic heat source with constant temperature T_D centred at (x_0, y_0, z_0) and parallel to the detachment[10] to mimic the driving heat source. Its geometry and location are shown in Extended Data Fig. 3; (3) a cylindric shallow tectonic structure (i.e. pipe) with radius R_D and permeability k_D penetrates the crust and intersects with the detachment. The offsets between the centre of the pipe and the heat source are $(\Delta x, \Delta y, \Delta z)$, and the distance from the pipe centre to the edge of the heat source is $d(\theta)$ (see Extended Data Fig. 3b).

Based on the simplified model configuration, the hydrostatic pressure at the intersection of the pipe's central line and the bottom surface of the detachment (red point with green edge in Extended Data Fig. 3a) can be expressed as,

$$p_0 = \rho_0 g H_{pipe} + \rho_U g \Delta H_0 \tag{9}$$

where $\Delta H_0 = H_{hs} - H_{pipe}$ denotes the distance between the bottom centre (green point with cyan edge in Extended Data Fig. 3a) of pipe and the intersection. ρ_0 and ρ_U denote density of cold fluid (i.e. sea water) and upwelling hot fluid, respectively. g is the gravitational acceleration. Similarly, the pressure at the heat source edge can be written as,

$$p(\theta) = \rho_0 g H(\theta) = \rho_0 g (H_{hs} - R_x \cos\theta \sin\alpha) \tag{10}$$

where H_{hs} represents the depth of the heat source centre below the seafloor, R_x the semi-axis length of the heat source ellipse along the x-axis. Therefore, the pressure difference driving fluid from recharge zone (detachment fault zone) into reaction zone (above heat source) is approximately given by

$$\Delta p = p(\theta) - p_0 = (\rho_0 - \rho_U) g \Delta H_0 + \rho_0 g (\Delta x \tan\alpha - R_x \cos\theta \sin\alpha) \tag{11}$$

where Δx denotes offset of heat source centre and pipe centre along x-axis (similar meaning with $\Delta y, \Delta z$).

This pressure difference operates over distance $d(\theta)$ so that the magnitude of Darcy's velocity (or volume flux) from recharge zone to reaction zone can be expressed as

$$u \sim \frac{k_R}{\mu_U}\frac{\Delta p}{d(\theta)} \tag{12}$$

where μ_U denotes dynamic viscosity of the upwelling hot fluid and k_R is permeability of the reaction zone (i.e. detachment in this model setup). $d(\theta)$ is the distance between heat source boundary and pipe bottom centre (see the bluish dash-dotted line in Extended Data Fig. 3b) i.e.

$$d(\theta) = \sqrt{(R_x\cos\theta\cos\alpha - \Delta x)^2 + (R_x\cos\theta\sin\alpha - \Delta x)^2 + (R_z\sin\theta - \Delta z)^2} \tag{13}$$

Combining Equation 11, 12 and 13, the total mass flux into the reaction zone is expressed by a surface integration over the boundary of the reaction zone,

$$\begin{aligned} Q_{in} &\sim \int_0^{2\pi} u\rho_U dS = \int_0^{2\pi} u\rho_U H_R\sqrt{R_x^2\cos\theta + R_z^2\sin\theta}\,d\theta, \quad \left(\sqrt{R_x^2\cos\theta + R_z^2\sin\theta} \equiv R(\theta)\right) \\ &= \frac{k_R H_R \rho_U}{\mu_U}\int_0^{2\pi}\frac{\Delta p}{d(\theta)}R(\theta)d\theta \\ &= \frac{k_R H_R^2 \rho_U(\rho_0 - \rho_U)g}{\mu_U}\underbrace{\int_0^{2\pi}\frac{1}{d(\theta)\cos\alpha}R(\theta)d\theta}_{M_1} + \frac{k_R H_R \rho_U \rho_0 g}{\mu_U}\underbrace{\int_0^{2\pi}\frac{(\Delta x tan\alpha - R_x\cos\theta\sin\alpha)}{d(\theta)}R(\theta)d\theta}_{M_2} \end{aligned} \tag{14}$$

The discharge zone, represented by a cylindric pipe with permeability k_D, is much narrower than the recharge zone and thus represents a stronger total resistance to a given fluid volume flux. The discharge flow is driven by a vertical pressure gradient due to the density contrast of hot upwelling fluid and cold seawater. Similar to Equation 12, the discharge volume flux can be written as

$$w \sim \frac{g k_D(\rho_0 - \rho_U)}{\mu_U} \tag{15}$$

Consequently, the discharge mass flux flow out of the reaction zone is

$$Q_{out} \sim \rho_U w S_{pipe} = \frac{k_D R_D^2 \pi g \rho_U(\rho_0 - \rho_U)}{\mu_U} \tag{16}$$

where S_{pipe} is the cross-sectional area of the pipe zone. Considering the structure of convection cells and reaction zone, we note that fluid flows into the reaction zone with a volume flux u and total mass flux Q_{in}, and leaves it with volume flux w and total mass flux Q_{out}. We neglect any changes of fluid mass due to hydration and dehydration reactions[41]. Then combining Equation 14 and 16, the conservation of fluid mass in the reaction zone is expressed by the balance

$$k_D R_D^2 \sim \frac{k_R H_R^2}{\pi}M_1 + \frac{k_R H_R \rho_0}{\pi(\rho_0 - \rho_U)}M_2 \tag{17}$$

Following Equation 7 and 24 of Ref.[41], the total advective heat power through the discharge zone (pipe zone) is equal to the conductive heat power given by

$$E_{cond} \sim g k_D F_U \pi R_D^2 \tag{18}$$

where $F_U = \rho_f(H_f - H_0)(\rho_f - \rho 0)/\mu_f$ is defined as the thermodynamic variable *fluxibility*, where H_0 represent specific enthalpy of cold fluid (sea water). Combining Equation 17 and 18, the permeability of the reaction zone, k_R, can be expressed in terms of E_{cond} and H_R,

$$k_R \sim \frac{E_{cond}}{\pi g F_U} \frac{\pi(\rho_0 - \rho_U)}{{H_R}^2 M_1(\rho_0 - \rho_U) + H_R \rho_0 M_2} \tag{19}$$

While H_R can be expressed in terms of E_{cond} and driving temperature T_D by applying the energy conservation law (see Eq. 7 of Ref[41])

$$H_R \sim \frac{\pi R_x R_z \lambda(T_D - T_U)}{E_{cond}} \tag{20}$$

Finally, substituting Equation 20 into Equation 19, we obtain the total advective heat power E_{cond} as a function of reaction (detachment) zone permeability (k_R), driving temperature (T_D) (i.e. heat source temperature), geometry (R_x, R_z) and location ($\Delta x, \Delta z$) of the heat source. The scaling analysis results are shown in Extended Data Fig. 4-5.

Data availability

The ship-based and the AUV bathymetric data are available at https://doi.pangaea.de/10.1594/PANGAEA.899415[57]. The P-wave tomography[36] data and micro-earthquake[5] data can be requested from the authors. The 3-D hydrothermal simulations were computed using the open-source code HydrothermalFoam V1.0[38](www.hydrothermalfoam.info). Model result data, model setup files and all related scripts can be found at Figshare (doi:10.6084/m9.figshare.16622053).

[51] Jasak, H. *Error analysis and estimation for the finite volume method with applications to fluid flows.* Ph.D. thesis, Imperial College of Science, Technology and Medicine (1996).

[52] Pye, J. Freesteam project. https://sourceforge.net/projects/freesteam/ (2010).

[53] Guo, Z. *et al.* Anhydrite-Assisted Hydrothermal Metal Transport to the Ocean FloorInsights From Thermo-Hydro-Chemical Modeling. *J. Geophys. Res. Solid Earth* **125**, e2019JB019035, DOI: https://doi.org/10.1029/2019JB019035 (2020).

[54] Floyd, J., Mutter, J., Goodliffe, A. & Taylor, B. Evidence for fault weakness and fluid flow within an active low-angle normal fault. *Nature* **411**, 779–783, DOI: 10.1038/35081040 (2001).

[55] Ludwig, R. J., Iturrino, G. J. & Rona, P. A. 23. Seismic velocity-porosity relationship of sulfide, sulfate, and basalt samples from the TAG hydrothermal mound. *Proc. Ocean. Drill. Program, Sci. Results; Tex. A & M Univ. Coll. Station. TX, USA* **158**, 313–328, DOI: 10.2973/odp.proc.sr.158.225.1998 (1998).

[56] McCaig, A. M. & Harris, M. Hydrothermal circulation and the dike-gabbro transition in the detachment mode of slow seafloor spreading. *Geology* **40**, 367–370, DOI: 10.1130/G32789.1 (2012).

[57] Petersen, S. Bathymetric data products from AUV dives during METEOR cruise M127 (TAG Hydrothermal Field, Atlantic), DOI: 10.1594/PANGAEA.899415 (2019).

Acknowledgements

This research was supported by National Key R&D Program of China (no. 2018YFC0309901), COMRA Major Project(no. DY135-S1-01-01), German Science Foundation (DFG) (no. 428603082), Oceanic Interdisciplinary Program of Shanghai Jiao Tong University (SL2020MS033), Talent Cultivation Project of Zhejiang Association for Science and Technology (SKX201901). HLRN cluster provided parallel computing.

Author contributions

L.H.R. and C.T. initiated the study. Z.G. and L.H.R. developed the 3D numerical model. Z.G. carried out the 3D simulations, did the post-processing and data visualizations. Z.G. and L.H.R. wrote the initial manuscript, S.P., C.R.G., B.I., J.H. and C.T. discussed and contributed geological implications. Figures and text were edited and improved by all authors.

Competing interests

The authors declare no competing interests

Additional information

Supplementary information is available for this paper.
Correspondence and requests for materials should be addressed to L.H.R.

Extended figures

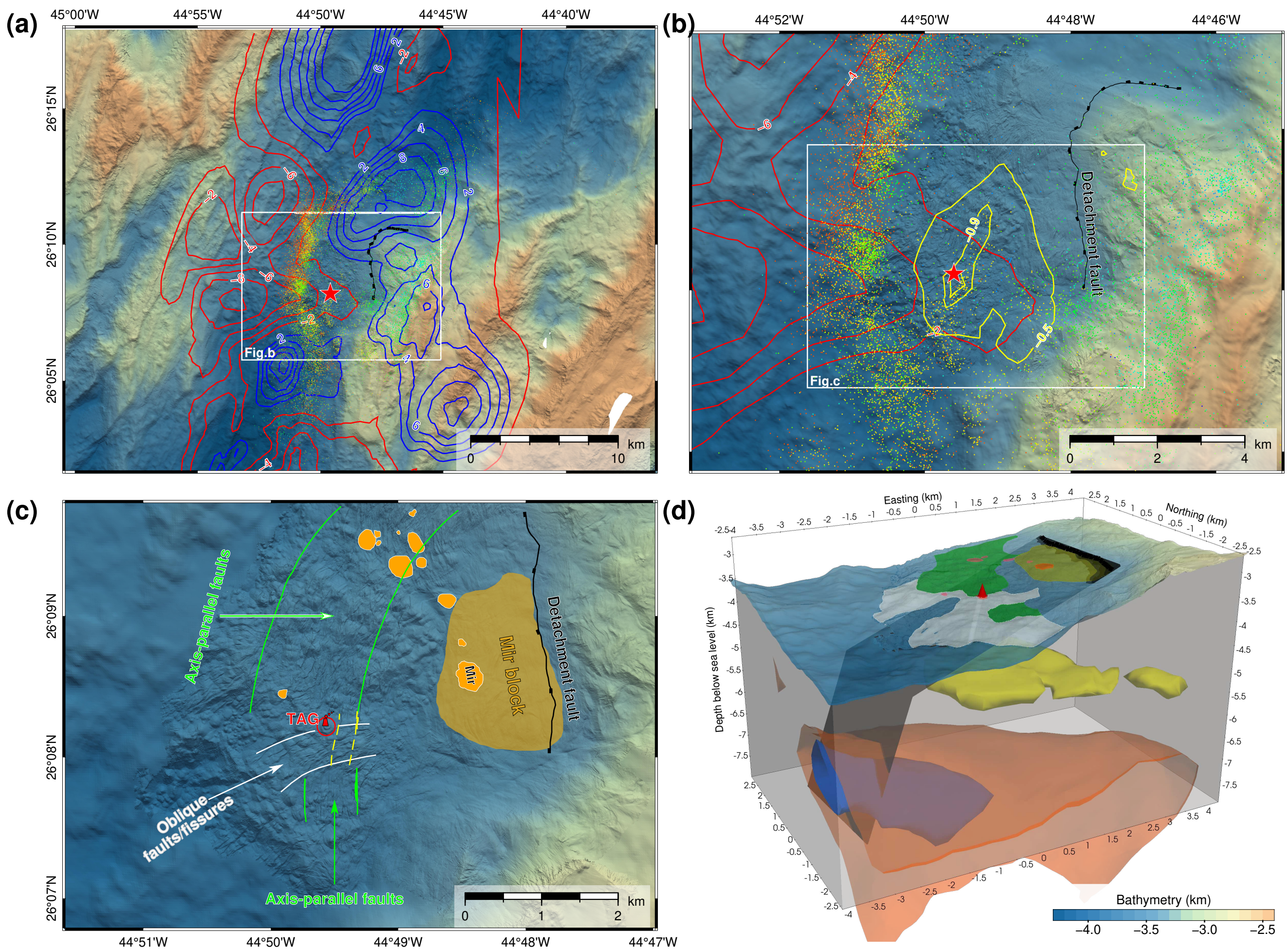

Extended Data Fig. 1: Geophysical data. (a) Bathymetry of TAG segment with contour lines of P-wave velocity variation at depth of 3 km below seafloor. Low and high velocity zones are marked by red and blue contour lines, respectively. White box represent range of fig.b. Color-scaled dots are microearthquake locations. The black line (also in Fig. b) represents termination of the extended detachment fault. TAG mound are marked by red star (same as Fig. b) (b) Close-up of the area marked by white box in (a). High resolution AUV bathymetry shows detachment fault. The red and yellow contour lines represent variation (%) and vertical gradient (1/s) of P-wave velocity at depth of 3 km and 1.75 km below seafloor, respectively. The white box denotes range of fig.c. (c) Close-up of the 3D model area. The TAG mound is marked by red circle, the Mir Mound and other hydrothermal mounds are shown by polygons in orange. The dashed yellow lines represent reactivated faults[32]. Axis-parallel faults area and oblique faults/fissures area are outlined by green lines and white lines, respectively. (d) 3D view of (c) with integrated geophysical data. Axis-parallel and oblique faults area are represented by green and white polygons. Yellow volumes below seafloor represent contour surface of -0.5 1/s of vertical gradient of P-wave velocity. Blue and orange volume represent contour surface -3% and -5% of P-wave velocity variation, respectively. Black incline surface underneath seafloor denotes detachment fault zone inferred from both 3D tomography data and micro-earthquake data.

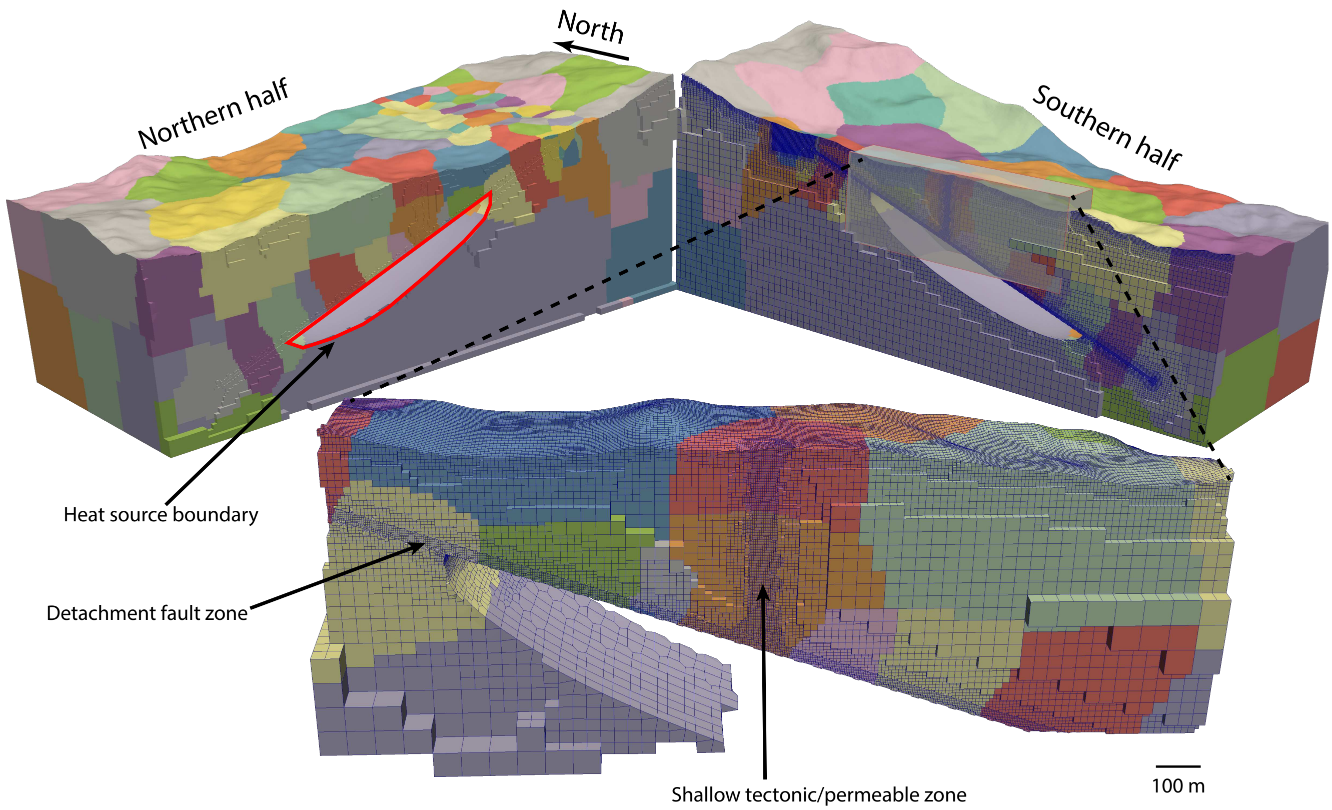

Extended Data Fig. 2: 3D domain decomposed into 150 subdomains. Each subdomain is represented by a different colour. The maximum cell size is $\sim$ 50 m and the minimum cell size is $\sim$ 5 m. To better visualize the geometry and mesh structures, the 3D modeling domain is divided into two parts, one is northern half part and the other one is southern half part.

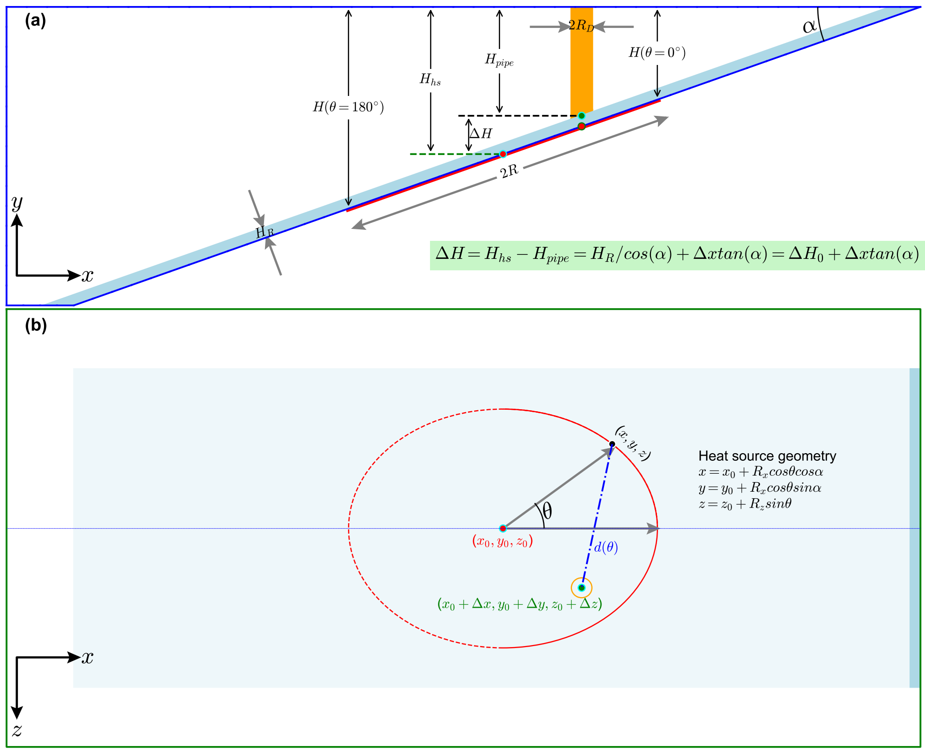

Extended Data Fig. 3: Model geometry of detachment fault controlled hydrothermal system. Assuming the geometry of heat source boundary patch is ellipse with semi-major axis R_x and semi-minor R_z, and semi-major axis is parallel with x axis of the coordinate system.

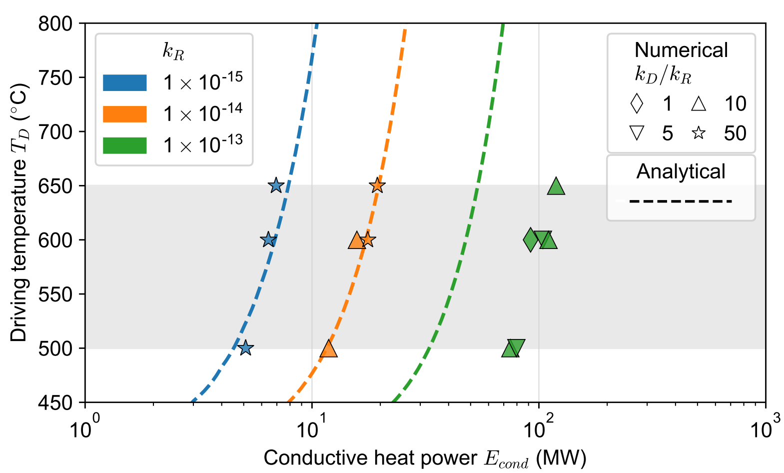

Extended Data Fig. 4: Comparison of semi-analytical and 3-D numerical model predictions on hydrothermal power output. The dashed lines display the analytic relationship (see methods) between conductive heat input (E_{cond}), permeability of reaction zone (k_R), and driving temperature(T_D). The numerical models share the same parameters for geometry (see Extended Data Fig.3) and boundary conditions with the simplified analytic model but also include effects of variations in discharge zone permeability (k_D), shown as differing symbols. Power output mainly scales with reaction zone permeability and driving temperature, which both control thermal boundary layer thickness. Predictions of analytical and numerical models deviate at high permeability values, most likely because the analytical model assumes radial symmetry while the 3-D model evolves, without such constraints, to a nearly but not perfect symmetric upflow zone.

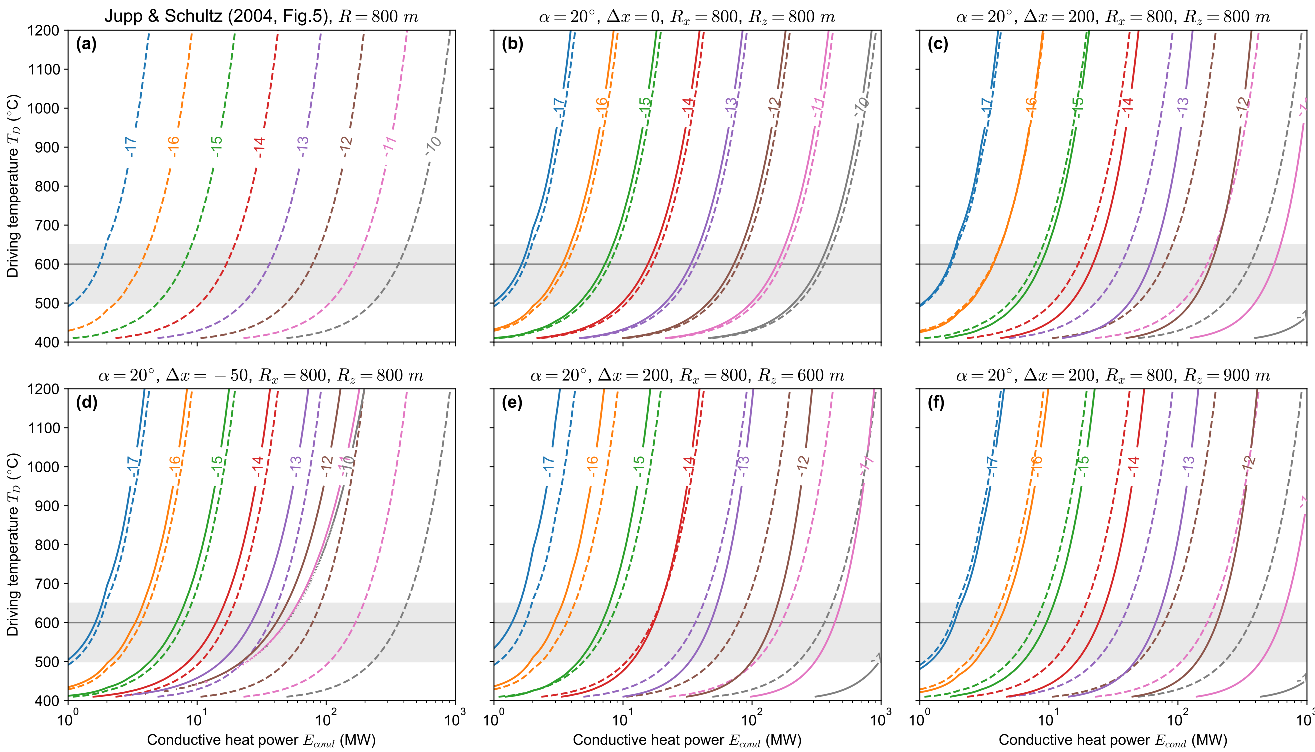

Extended Data Fig. 5: Scaling analysis results of detachment-pipe model. Solid and dashed lines represent contours of k_R of Jupp & Schultz(2004)[41] and our models with different parameters, respectively. Parameters are shown on the top side of the subplots. (a) Reproduced result of Jupp & Schultz(2004)[41] model which is a special case of detachment-pip model when $\alpha = 0$. (b) Result of reference model. (c) and (d) show how conductive heat power depend on Δx by comparing with (b). For the same permeability of detachment and a fixed heat source, the conductive heat power will increase with pipe moving more close to the upper edge of the heat source. (e) and (f) show how E_{cond} depend on R_z and R_x by comparing with (c), respectively. Spatial extent of the heat source is positively proportional to the conductive heat power. Parameters used in these calculations are:

$g = 9.8m/s^2, \lambda = 2W/m/K, T_U = 400°C, \phi = 0.1, F_U = 1.2 \times 10^{16} J\ s/m^5, \rho_0 = 1016, \rho_U = 475\ kg/m^3$.

Supplementary Files

This is a list of supplementary files associated with this preprint. Click to download.

- Recharge.mp4
- Discharge.mp4
- SupplementaryInformation.pdf